Available online at www.sciencedirect.com
ScienceDirect
Trans. Nonferrous Met. Soc. China 30(2020) 3307−3321
Transactions of Nonferrous Metals Society of China
www.tnmsc.cn

Microstructure and compression properties of fine Al_2O_3 particles dispersion strengthened molybdenum alloy

Tie-long SUN[1], Liu-jie XU[1], Shi-zhong WEI[2], Kun-ming PAN[1], Wu-hui LI[1], Yu-cheng ZHOU[2], Zhi-min HUANG[3]

1. Henan Key Laboratory of High Temperature Structural and Functional Materials, Henan University of Science and Technology, Luoyang 471003, China;
2. National Joint Engineering Research Center for Abrasion Control and Molding of Metal Materials, Henan University of Science and Technology, Luoyang 471003, China;
3. China National R&D Center for Tungsten Technology, Xiamen Tungsten Corporation, Ltd., Xiamen 361000, China

Received 10 March 2020; accepted 7 September 2020

Abstract: The Mo alloys reinforced by Al_2O_3 particles were fabricated by hydrothermal synthesis and powder metallurgy. The microstructures of Mo−Al_2O_3 alloys were studied by using XRD, SEM and TEM. The results show that Al_2O_3 particles, existing as a stable hexagonal phase (α-Al_2O_3), are uniformly dispersed in Mo matrix. The ultrafine α-Al_2O_3 particles remarkably refine grain size and increase dislocation density of Mo alloys. Moreover, a good interfacial bonding zone between α-Al_2O_3 and Mo grain is obtained. The crystallographic orientations of the interface of the Al_2O_3 particles and Mo matrix are $[\bar{1}11]_{\alpha\text{-}Al_2O_3}//[\bar{1}11]_{Mo}$ and $(1\bar{1}2)_{\alpha\text{-}Al_2O_3}//(0\bar{1}1)_{Mo}$. Due to the effect of secondary-phase and dislocation strengthening, the yield strength of Mo−2.0vol.%Al_2O_3 alloy annealed at 1200 °C is approximately 56.0% higher than that of pure Mo. The results confirm that the addition of Al_2O_3 particles is a promising method to improve the mechanical properties of Mo alloys.

Key words: Mo−Al_2O_3 alloys; hydrothermal synthesis; interface; compression test; dispersion strengthening

1 Introduction

High-temperature structural materials with excellent performance are urgently required as various industries are further developed. Mo, an important and prominent element among the refractory metals, is favored by researchers [1−3]. Mo and its matrix composites are extensively used in aerospace, metallurgy, nuclear power, military and other high-tech fields due to their high melting point, high creep resistance, high thermal conductivity and low coefficient of thermal expansion [4−7]. However, as a representative body-centered cubic (bcc) transition metal, Mo also presents several major drawbacks, such as low-temperature brittleness and low recrystallization temperature at room temperature (RT), and these limitations restrict its application fields [8−10]. Thus, it is vital to strengthening/toughening of Mo alloys and knowledge of the failure mechanism of these alloys at work is necessary.

Grain refinement is an effective method to simultaneously improve the strength and ductility of Mo alloys [1]. Indeed, a considerable amount of research on this topic has been conducted in recent decades [11,12]. Dispersion strengthening by doping with oxides can effectively improve the strength and ductility of Mo alloys and enhance their deep processing [5,13,14]. Introduction of oxide dispersion-strengthened phases can refine grains and hinder grain growth and dislocation

Foundation item: Projects (U1704152, U1804124) supported by the National Natural Science Foundation of China; Project (174100510012) supported by Plan for Scientific Innovation Talent of Henan Province, China
Corresponding author: Liu-jie XU; Tel: +86-379-64270020; E-mail: wmxlj@126.com
DOI: 10.1016/S1003-6326(20)65463-2

motion [15]. Doping of rare-earth oxides (e.g., La_2O_3, Y_2O_3, CeO_2 and ThO_2) into the Mo matrix is a traditional approach used to compensate for the deficiency of the metal [16]. YANG et al [17] introduced trace amounts of nanosized La_2O_3 particles to a Mo matrix via the solid–liquid doping method and revealed a tensile elongation to failure of 42% at RT. Because rare-earth elements are non-renewable resources, however, the use of metal−ceramic oxides (e.g., ZrO_2, Al_2O_3) for doping into Mo alloys has been considered [6,8,9]. CUI et al [18,19] successfully synthesized Mo−ZrO_2 alloys via the hydrothermal method and found that the respective hardness and strength of these alloys are 40% and 35% higher than those of pure Mo. Unfortunately, despite such successes, the crystal transformation of *m*-, *t*-, *c*-ZrO_2 at high temperatures decreases the properties of Mo alloys. Al_2O_3 presents many advantages, such as high elastic modulus, low density, excellent bio-compatibility, oxidation resistance and stability at high temperature [20,21]. ZHOU et al [22] developed Al_2O_3-doped Mo sheets via the hydrothermal method and observed a tensile strength 23% and 62% higher than those of pure Mo sheets at RT and high temperature, respectively. Although Mo materials are used in many high-tech fields, such as nuts and flanges, most available research on Mo alloys is focused on their tensile and compressive properties at high temperature; the compressive mechanical property of these alloys at RT has been given little attention [23,24].

Molybdenum, as indenter, nut, nozzle and so on, needs excellent mechanical properties. In the current work, Mo alloys doped with nanosized Al_2O_3 particles are prepared by the hydrothermal and powder metallurgy methods. The micro-structure and mechanical properties of Mo−Al_2O_3 alloys annealed at different temperatures are investigated, and the effects of Al_2O_3 in the Mo matrix on the resulting deformation and failure mechanisms are assessed.

2 Experimental

2.1 Preparation of Mo−Al_2O_3 samples

Mo−Al_2O_3 alloys with 0, 0.4, 0.8, 1.2, 1.6 and 2.0 vol.% Al_2O_3 addition were fabricated by hydrothermal synthesis (Table 1). The self-assembly of Mo alloys is illustrated in Fig. 1. Commercial $(NH_4)Mo_4O_{13}·2H_2O$ (99.9% in purity) was dissolved in distilled water and the pH was adjusted to be 1.0 by HNO_3 solution with stirring. Commercial $Al(NO_3)·9H_2O$ (99.9% in purity) and $CO(NH_2)_2$ (99.9% in purity) were dissolved in distilled water and the pH of the solutions was adjusted to be 9.0. These solutions were respectively placed into autoclave, which were then sealed and heated at 170 °C for 15 h. Subsequently, the mixture of two kinds of reaction products was stirred for over 2 h using an electric mixer and dried at 120 °C in an oven. The obtained dry gels were calcined at 550 °C for 2 h and then doubly reduced

Table 1 Chemical composition of samples (vol.%)

Sample No.	Mo	Al_2O_3
0	100	0
1	99.6	0.4
2	99.2	0.8
3	98.8	1.2
4	98.4	1.6
5	98.0	2.0

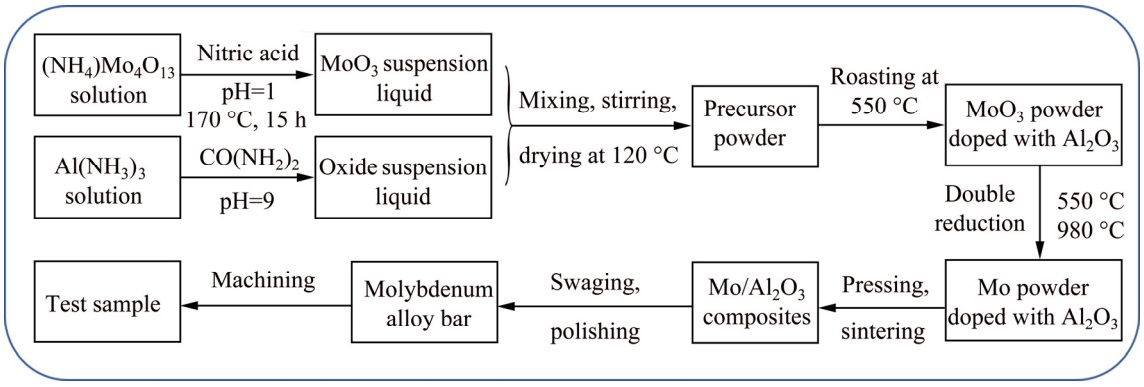

Fig. 1 Preparation process of Mo−Al_2O_3 alloys

under dry hydrogen in a tube furnace at 550 and 980 °C to form the Mo−Al_2O_3 powders. Finally, the compound powders were statically cold-pressed into cylindrical compacts with a diameter of 20 mm under a pressure of 280 MPa for 15 min and sintered at 1920 °C for 3 h in a hydrogen atmosphere. The sintered compacts were heated at 1400 °C for 15 min in a Mo wire furnace (ZMY−50−15), and then swage-deformed to exceed 84% by multistep rotation to form a diameter of 8 mm after surface polishing. Cylindrical specimen with dimensions of *d*8 mm × 12 mm was obtained by wire electrical discharge machining.

2.2 Microstructural characterization and properties measurement

The powder morphologies and microstructure of Mo alloys were observed by scanning electron microscopy (SEM, VEGA−SBH), transmission electron microscopy (TEM, JEM−2100) and high-resolution electron microscopy. The size of the Mo−Al_2O_3 powders was analyzed by a laser light scattering analyzer (OMCC−LS909). Phase compositions were analyzed by using energy-dispersive X-ray spectrometry (EDS) and X-ray diffraction (XRD, Brux D8). Grain sizes were measured by the linear intercept method. RT compression tests were executed on a SHIMADZU AG−I 250 kN at a constant train rate of 1.39×10^{-3} s^{-1}, and the sizes of samples are 8 mm in diameter and 12 mm in length. Compression samples were annealed at 850 and 1200 °C, respectively. And these samples were prepared for each set of tests. In the current work, the average yield strength was calculated on the basis of the results of three compression specimens.

2.3 Nano-indentation testing

Nano-indentation tests were performed by using a Keysight G200 TriboIndenter system equipped with a Berkovich indenter. Indentation marks were made on the polished samples using an applied depth of 2000 nm, strain rate of 0.05 mN/s, allowable drift rate of 0.90 nm/s, and dwell time of 10 s. Twelve points were tested for each sample under the same conditions, and the average nano-hardness (h) and reduced elastic modulus (E) were calculated.

3 Results and analysis

3.1 Morphology of composite powders

The SEM morphologies of different powders after double reduction are shown in Fig. 2. The size of Mo powders decreases with increasing Al_2O_3 content, and similar morphologies of nearly spherical particles are observed (Fig. 2). The characteristic parameters of Mo−Al_2O_3 powders are summarized in Table 2. The mean particle size (D_{50}) and mean volume diameter (D(4,3)) of the powders first decrease and then slightly increase with increasing Al_2O_3 content. The specific surface area (SSA) of the powders increases with increasing D_{50} and D(4,3). The minimum mean particle size is

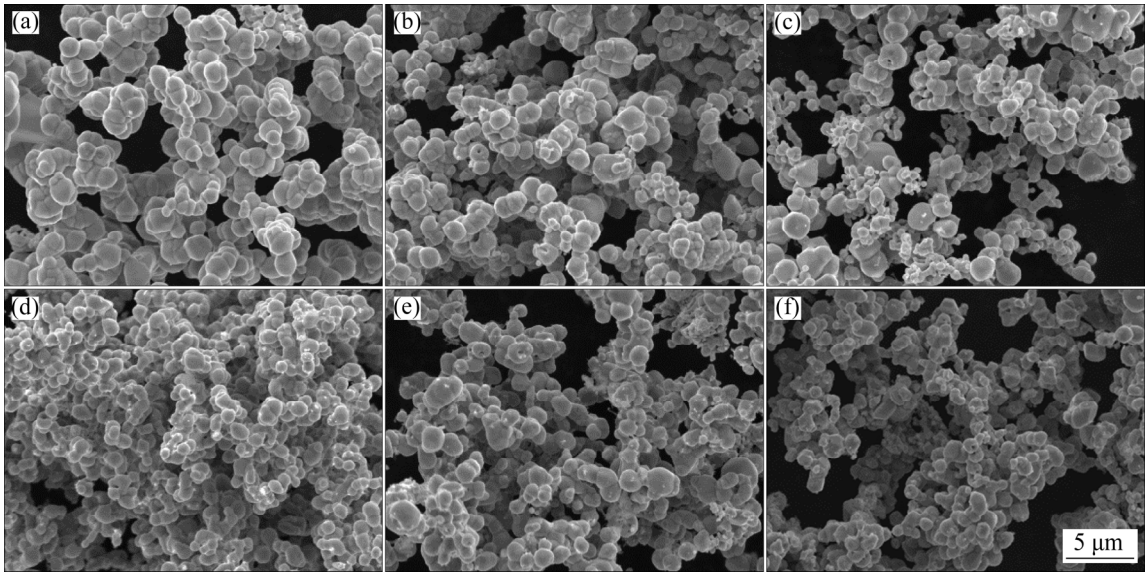

Fig. 2 Morphologies of different powders: (a) Pure Mo; (b) Mo−0.4vol.%Al_2O_3; (c) Mo−0.8vol.%Al_2O_3; (d) Mo−1.2 vol.%Al_2O_3; (e) Mo−1.6vol.%Al_2O_3; (f) Mo−2.0 vol.%Al_2O_3

Table 2 Characteristic parameters of size distribution of powders

Al_2O_3 content/ vol.%	D_{50}/ μm	$D(4,3)$/ μm	SSA/ ($m^2 \cdot g^{-1}$)
0	4.38	4.61	1.7
0.4	3.49	4	2.01
0.8	2.35	2.46	2.78
1.2	2.05	2.13	3.21
1.6	2.2	2.41	2.95
2.0	2.23	2.42	2.94

2.05 μm and the maximum SSA is 3.21 m^2/g when the Al_2O_3 content is 1.2 vol.%.

Figure 3 illustrates the particle size distributions of Mo alloy powders doped with Al_2O_3 particles, including frequency distribution curve and cumulative distribution. The mean size of the Mo powders evidently decreases with increasing Al_2O_3 content. Therefore, Al_2O_3 can effectively refine and homogenize composite powders. However, the particle size of the Mo powders only slightly increases when the Al_2O_3 content exceeds 1.6 vol.% (Fig. 4), likely because of an increase in

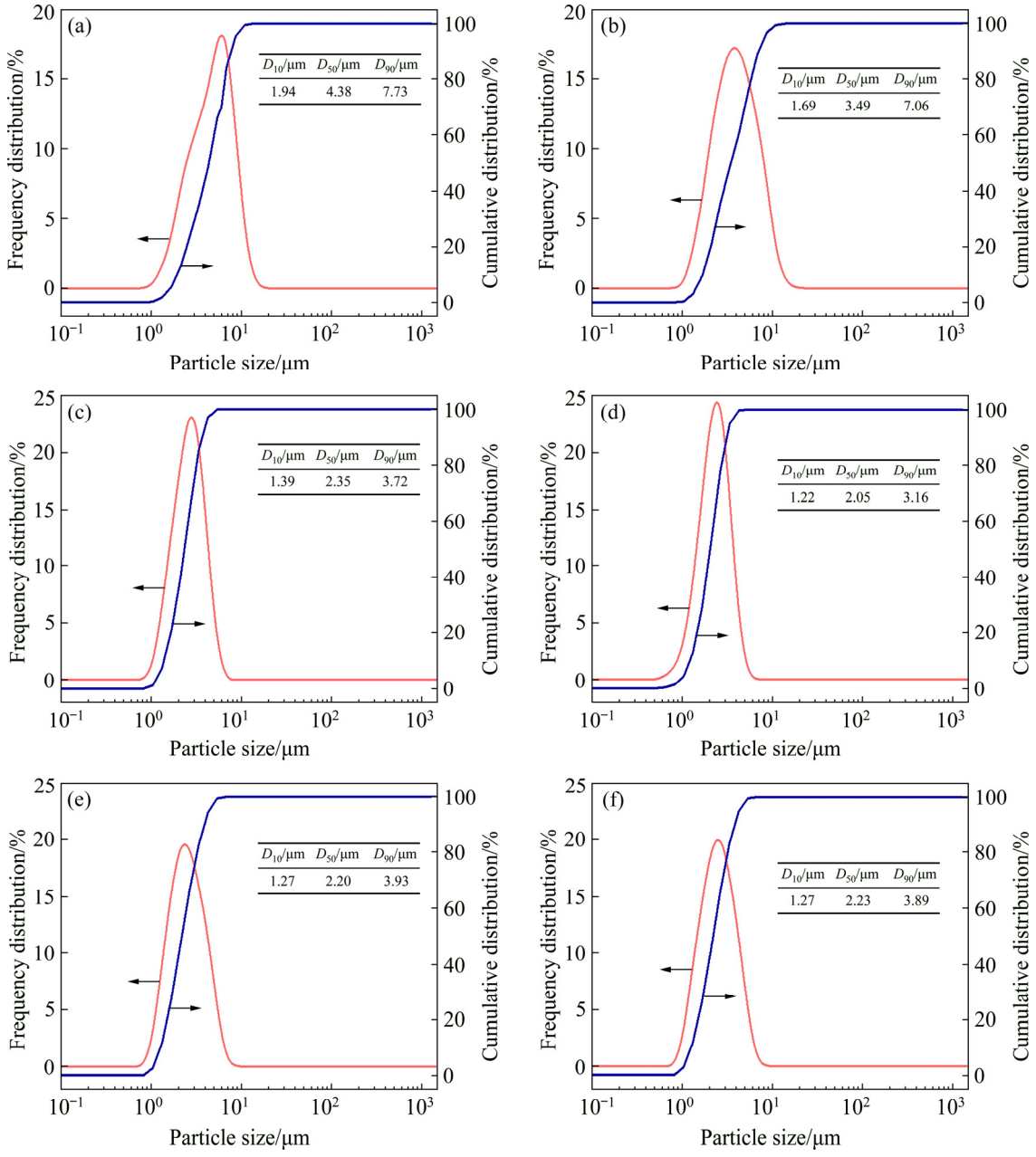

Fig. 3 Particle size distributions of molybdenum powders doped with different contents of Al_2O_3: (a) Pure Mo; (b) Mo−0.4vol.%Al_2O_3; (c) Mo−0.8vol.%Al_2O_3; (d) Mo−1.2vol.%Al_2O_3; (e) Mo−1.6vol.%Al_2O_3; (f) Mo−2.0 vol.%Al_2O_3

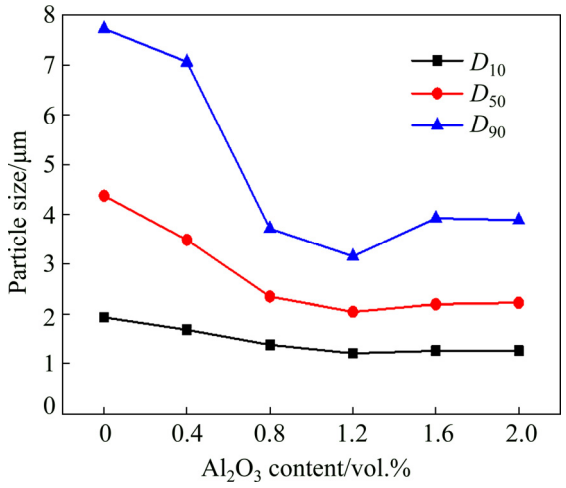

Fig. 4 Variation trend of particle size distribution parameters of powders

particle aggregation. In addition, the change in the cumulative size distributions of all Mo alloy powders reveal a "V" shape, which indicates that the Mo−1.2vol.%Al_2O_3 powder has the best scale uniformity among the samples obtained (Fig. 4).

3.2 Microstructure of Mo alloys

Figure 5 shows SEM images of the microstructures of the Mo alloys obtained in the radial direction after sintering. The size of Mo grains decreases with increasing doping amount of Al_2O_3. The small grayish-white spherical particles observed in these images are identified as Al_2O_3 (Figs. 5(c, d)) through EDS analysis (Fig. 5(e)). These particles are uniformly distributed on the Mo grain boundary and the matrix, thus effectively

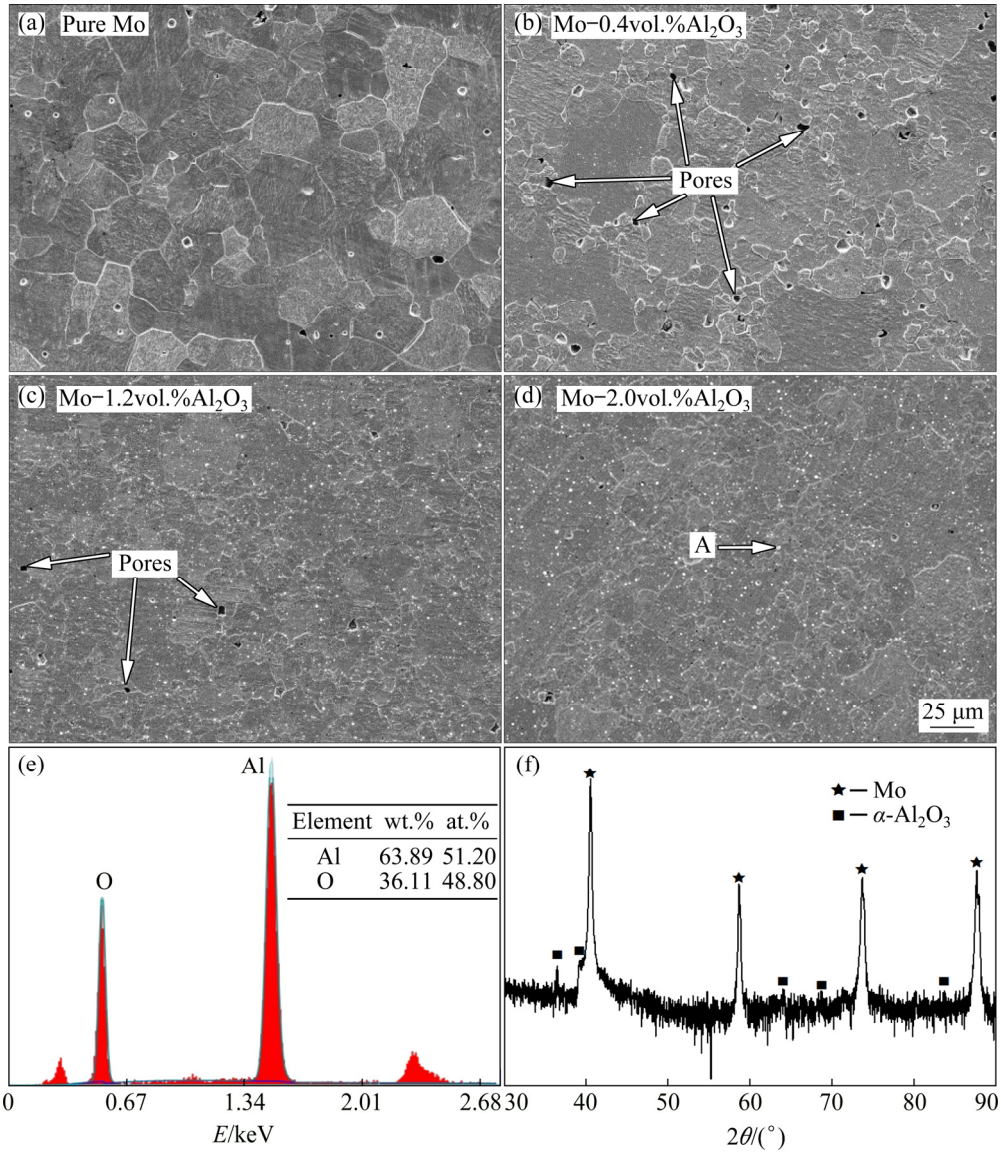

Fig. 5 SEM micrographs of sintered compact (a−d), EDS spectrum of Particle A (e), and XRD pattern of Mo−2.0vol.%Al_2O_3 (f)

suppressing grain growth during sintering. The number of micropores decreases with increasing Al_2O_3 content (Figs. 5(b−d)), likely because the effect of grain refinement is not evident when only a small amount of Al_2O_3 particles are doped into the Mo matrix. Moreover, the uniformly distributed Al_2O_3 particles prevent Mo grain boundaries from forming micropores during sintering, similar to observations in W alloys [25], and can adsorb impurity elements. The concentration of impurity elements at Mo grain boundaries decreases with increasing doping amount of Al_2O_3 (Fig. 5(d)). The XRD patterns of the Mo−Al_2O_3 alloys are shown in Fig. 5(f) and the sintered alloys primarily consist of Mo and α-Al_2O_3.

Figure 6 illustrates representative SEM-BSE images of the microstructures of Mo alloys swaged and annealed at 1200 °C. The grain size of Mo alloy annealed at 850 °C has no obvious change compared with that of rotary swaging state, and the SEM image is not shown in here. The grain sizes of Mo decrease with increasing Al_2O_3 content. Specific changes in Mo grain size are shown in Fig. 7. As the Al_2O_3 content increases from 0 to 2.0 vol.%, the grain size of Mo alloys obtained at RT and after annealing at 850 °C decrease from approximately 27 to 2.5 μm, and the Mo grain size of the alloy annealed at 1200 °C decreases from approximately 55 to 3.5 μm. The grain size of the Mo−2.0vol.%Al_2O_3 alloy is much smaller than that of the pure Mo alloy, which indicates that Al_2O_3 particles can effectively refine the grain size of Mo−Al_2O_3 alloys. Moreover, micropores are often found adjacent to the Al_2O_3 particles, which may be

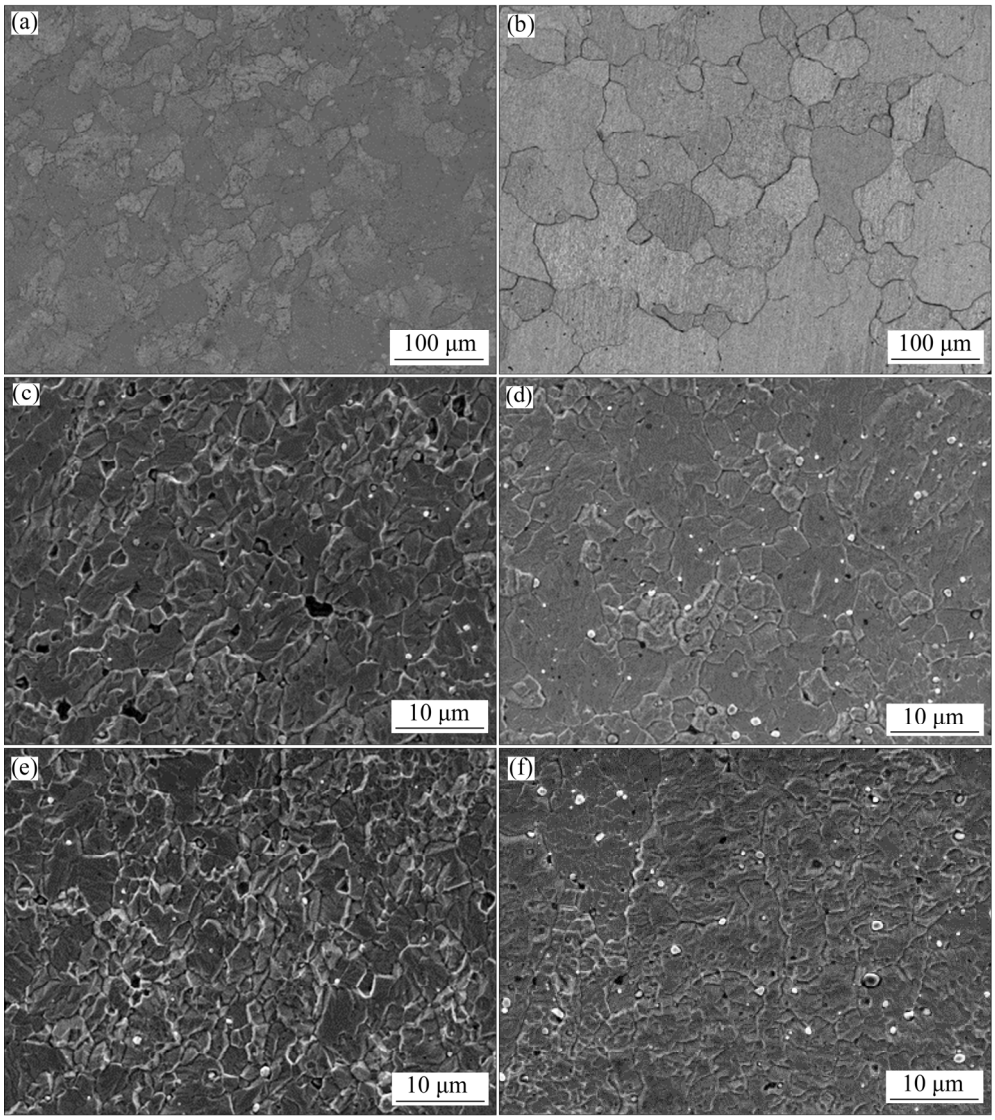

Fig. 6 SEM-BSE images of molybdenum alloys as-swaged (a, c, e) and after 1200 °C annealing (b, d, f): (a, b) Pure Mo; (c, d) Mo−1.2vol.%Al_2O_3; (e, f) Mo−2.0vol.%Al_2O_3

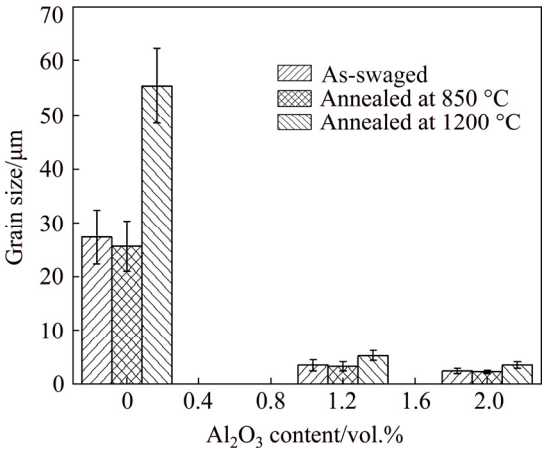

Fig. 7 Measured grain size of molybdenum alloys

due to mechanical mismatches between the Mo matrix and these particles during hot deformation. The twisted grain structure of pure Mo alloys formed by extrusion/forging is transformed into equiaxed grains by annealing at 1200 °C, thus indicating that pure Mo undergoes complete recrystallization. As shown in Fig. 7, the average grain size of the pure Mo alloy annealed at 1200 °C increases by 1 times compared with that of the pure Mo alloys as-swaged and after annealing at 850 °C. By comparison, the grain sizes of Mo−Al_2O_3 alloys obtained at different temperatures reveal minimal difference, which indicates that the recrystallization temperature of Mo alloy can be improved by doping with Al_2O_3 particles.

TEM investigations of the Mo−Al_2O_3 alloys reveal changes in dislocation structures resulting from annealing at different temperatures (Fig. 8). Dislocation accumulation decreases with increasing annealing temperature (Fig. 8). Many difficulties have been encountered when measuring the dislocation density (ρ) in alloys by TEM. The high density of dislocations in the Mo matrix and boundary shown in Fig. 8(a) is due to swage deformation, which results in work hardening. Moreover, as shown in Figs. 8(b, c), several dislocations could be found around Al_2O_3 particles, thus indicating that these particles can effectively block the expansion of dislocations and improve the mechanical properties of the resultant Mo−Al_2O_3 alloys. According to the Orowan dislocation bypass mechanism [26], as dislocations extend, the dislocation lines around Al_2O_3 particles meet, and the positive and negative dislocations cancel each other out, resulting in dislocation rings surrounding Al_2O_3 particles. The distribution and accumulation of dislocations are important factors affecting the properties of materials.

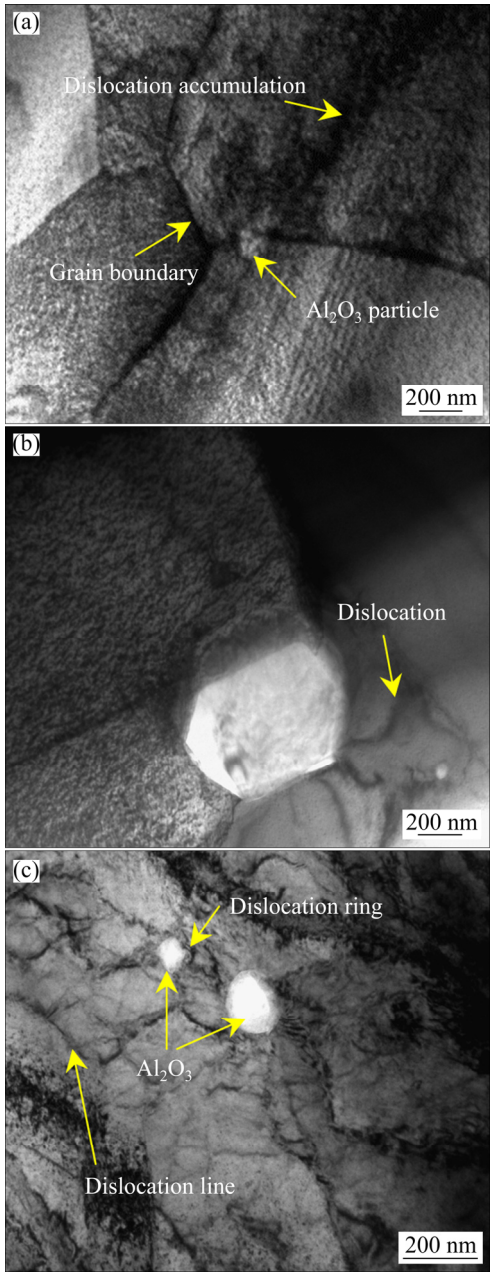

Fig. 8 TEM images of Mo−2.0vol.%Al_2O_3 alloys: (a) As-swaged; (b) Annealed at 850 °C; (c) Annealed at 1200 °C

TEM images of the samples are shown in Fig. 9 to show the microstructure of swaged Mo−Al_2O_3 alloys. The spherical Al_2O_3 particles, which are approximately a few tens to several hundreds of nanometers in size, are evenly distributed in the Mo matrix (Fig. 9(a)). The evident stacking faults of Al_2O_3 particles observed under

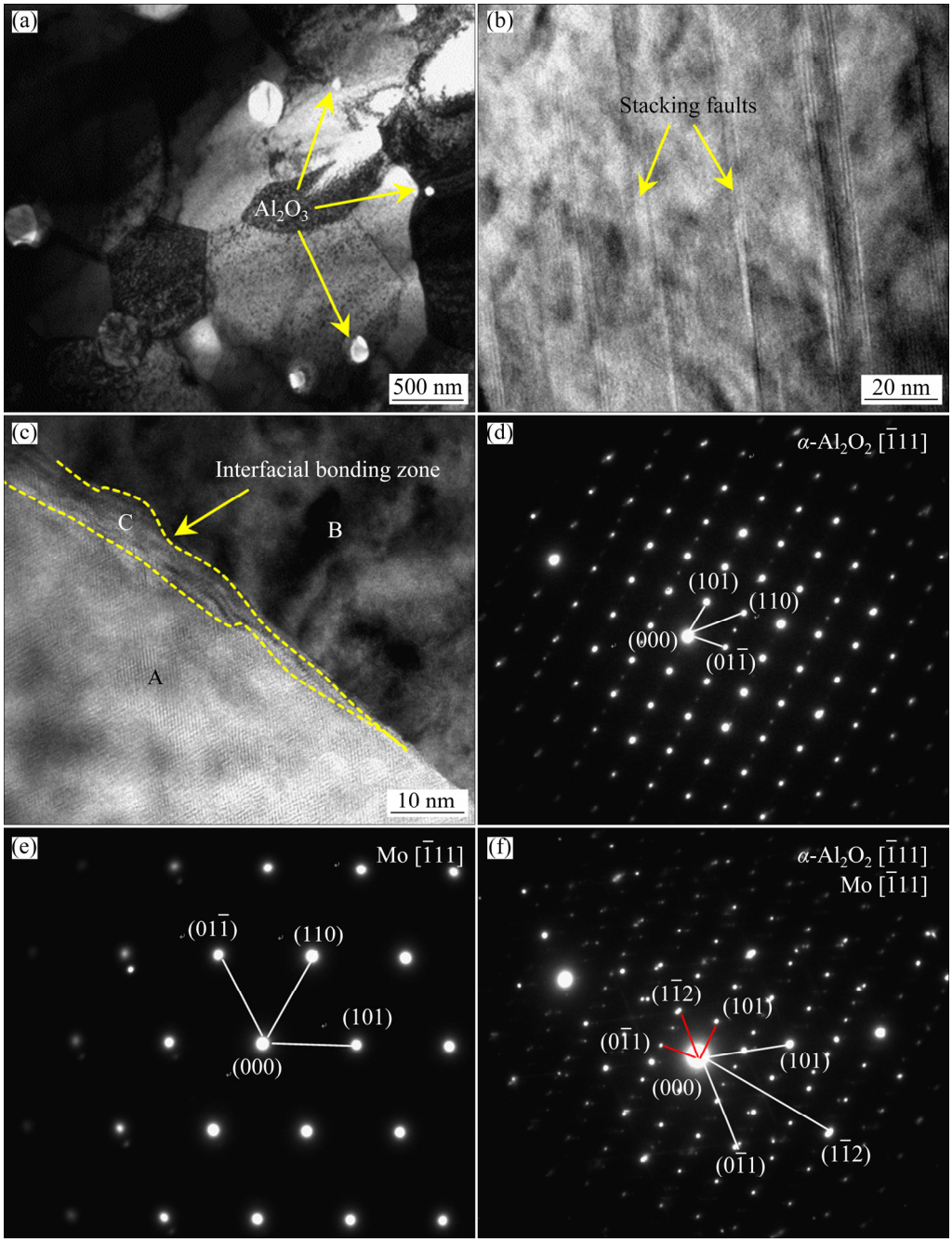

Fig. 9 Microstructures of swaged Mo−Al_2O_3 sample: (a) Morphology of Al_2O_3; (b) High magnification of Al_2O_3 particle; (c) HRTEM image of interface between Al_2O_3 and matrix; (d) Diffraction pattern for Area A; (e) Diffraction pattern for Area B; (f) Diffraction pattern for Area C

high magnification may be related to the hexagonal close-packed (hcp) atomic stacking mode, which is characteristic of α-Al_2O_3 (Fig. 9(b)). And the stacking faults in Al_2O_3 may be caused by particles growth during sintering, as reported by XU et al [27]. In addition, a clear interfacial bonding zone is found between Al_2O_3 and the Mo matrix (Fig. 9(c)). No transition layer is found between Al_2O_3 and the Mo matrix in sintered Mo sheet doped with Al_2O_3, similar to findings by ZHOU et al [22]. The appearance of such an interface may be attributed to the plastic deformation produced by Mo grains. However, Al_2O_3 particles are hardly deformed during the hot rolling process, which leads to strong interactions between Mo atoms and the edges of Al_2O_3 particles to produce an amorphous interfacial bonding zone. Well-bonded interfaces between the strengthening phase and

matrix confirm that the alloys have good mechanical properties. The diffraction pattern of Area A shown in Fig. 9(d) confirms that the Al_2O_3 phases in the swaged compacts are α-Al_2O_3 with an hcp crystal structure along the $[\bar{1}11]$ direction. Figure 9(e) shows the diffraction pattern of the Mo matrix (Area B) with a bcc crystal structure in the $[\bar{1}11]$ direction. The diffraction pattern for Area C, which reflects the interfacial bonding zone between Al_2O_3 and the Mo matrix, shows a composite diffraction pattern (Fig. 9(f)), revealing crystallographic relationships of $[\bar{1}11]_{\alpha\text{-}Al_2O_3} // [\bar{1}11]_{Mo}$ and $(1\bar{1}2)_{\alpha\text{-}Al_2O_3} // (0\bar{1}1)_{Mo}$ according to mismatch theory proposed by TURNBULL and VONNEGUT [28].

3.3 Dislocation density, nano-hardness and elastic modulus of Mo alloys

Figure 10 shows the XRD patterns of Mo−2.0vol.%Al_2O_3 samples obtained under different conditions, and these patterns are used to estimate the dislocation density ρ of the Mo alloys. All of the peaks of {110}, {200}, {211} and {220} correspond to the bcc polymorph of Mo. However, due to the low intensity of the {200}, {211} and {220} peaks, only the high diffraction peak {110} is used in this work. Here, ρ can be quantified by the following relationship [29,30]:

$$\rho=\frac{3\sqrt{2\pi}\langle\varepsilon^2\rangle^{1/2}}{Db} \quad (1)$$

where $\langle\varepsilon^2\rangle^{1/2}$ is the micro-strain induced by crystal imperfections, D is the crystallite size, and b is the absolute value of Burgers vector, which is equal to 2.73 Å for 1/2⟨111⟩ type dislocations in pure Mo [31].

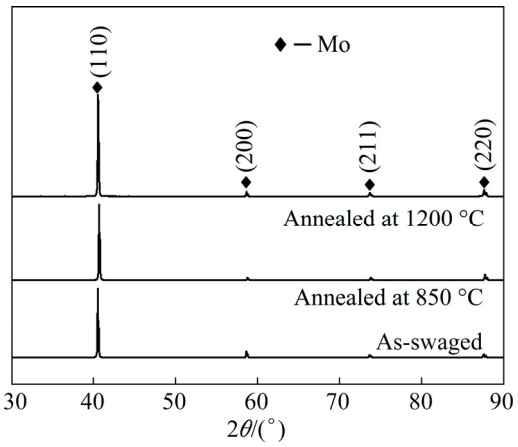

Fig. 10 XRD patterns of Mo−2.0vol.%Al_2O_3 alloys

The mean distance between dislocations l_d is estimated by using the following expression:

$$l_d=1/\sqrt{\rho} \quad (2)$$

The values of ρ and l_d calculated by using Eqs. (1) and (2) are summarized in Table 3. The ρ measured via the XRD method is not precise but can be adopted to indirectly analyze ρ [32]. As shown in Table 3, ρ decreases whereas l_d increases with increasing annealing temperature. Compared with the dislocation density of pure Mo under the same conditions, that of the Mo−2.0vol.%Al_2O_3 alloys increases by tens of times because doped Al_2O_3 particles can effectively prevent dislocation movement, resulting in dislocation pile-up and tangling. Thus, the dislocation slip requires greater stress than before, which improves the strength of the Mo alloy.

Table 3 Dislocation density (ρ) and mean distance between dislocations (l_d) of pure Mo and Mo−2.0vol.%Al_2O_3 under different conditions

Condition	Sample No.	Dislocation density, ρ/m^{-2}	Mean distance between dislocations, l_d/nm
As-swaged	0	1.01×10^{15}	100
	5	1.14×10^{17}	3
Annealed at 850 °C	0	7.05×10^{13}	120
	5	6.61×10^{14}	34
Annealed at 1200 °C	0	4.97×10^{12}	448
	5	2.94×10^{13}	184

Nano-indentation tests were carried out to explore the effect of Al_2O_3 particles on the mechanical properties of Mo alloys. The method of OLIVER and PHARR [33] was used to calculate the elastic modulus (E) of the indentations. The average values of E and nano-hardness (h) are shown in Fig. 11. Under the same conditions, the E and h of the Mo alloys show the similar change with increasing Al_2O_3 content. E and h of the Mo−Al_2O_3 alloys are higher than those of pure Mo. Improvements in E indicate that the Mo alloys are difficult to deform when subjected to an external force. Overall, the annealed Mo alloys show lower E and h compared with the as-swaged Mo alloys due to dislocation rearrangement and energy release during annealing.

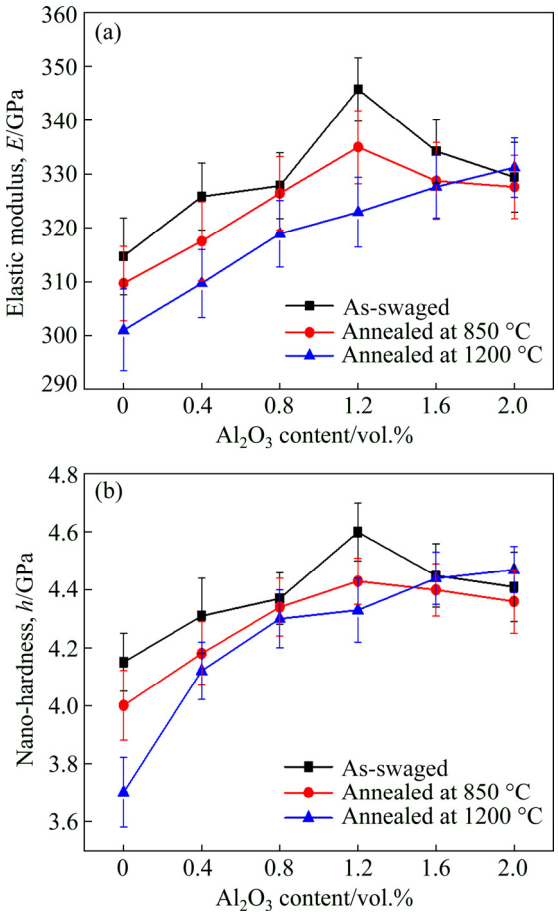

Fig. 11 Elastic modulus (a) and nano-hardness (b) of Mo−Al_2O_3 alloys under different conditions

3.4 Compressive properties and microstructure of Mo alloys after compression

Figure 12 shows the RT uniaxial compressive engineering stress−strain curves of the Mo−Al_2O_3 alloys at a strain rate of 1.39×10^{-3} s^{-1}. All of the Mo alloys show excellent ductility, which can delay the initiation and propagation of cracks. After yielding, the engineering stress of all Mo alloys continuously increases with increasing plastic strain (Fig. 12). All alloys display two deformation stages: the elastic deformation stage (Zone A) and the rapid increase in flow stress stage (Zone B) (Fig. 12(a)). Some samples show nonlinear elastic behavior or the "double yielding" phenomenon (yielding points 1 and 2) in Zone A, which has also been observed in the arc-melted Co−Fe alloys by ZHANG et al [34]. In general, the mechanism of double yielding in metal materials is complicated and has not yet been elucidated completely. The compression yield strength of all samples is illustrated in Fig. 13. With increasing Al_2O_3 content, yield strength of samples as-swaged and after 850 °C annealing first

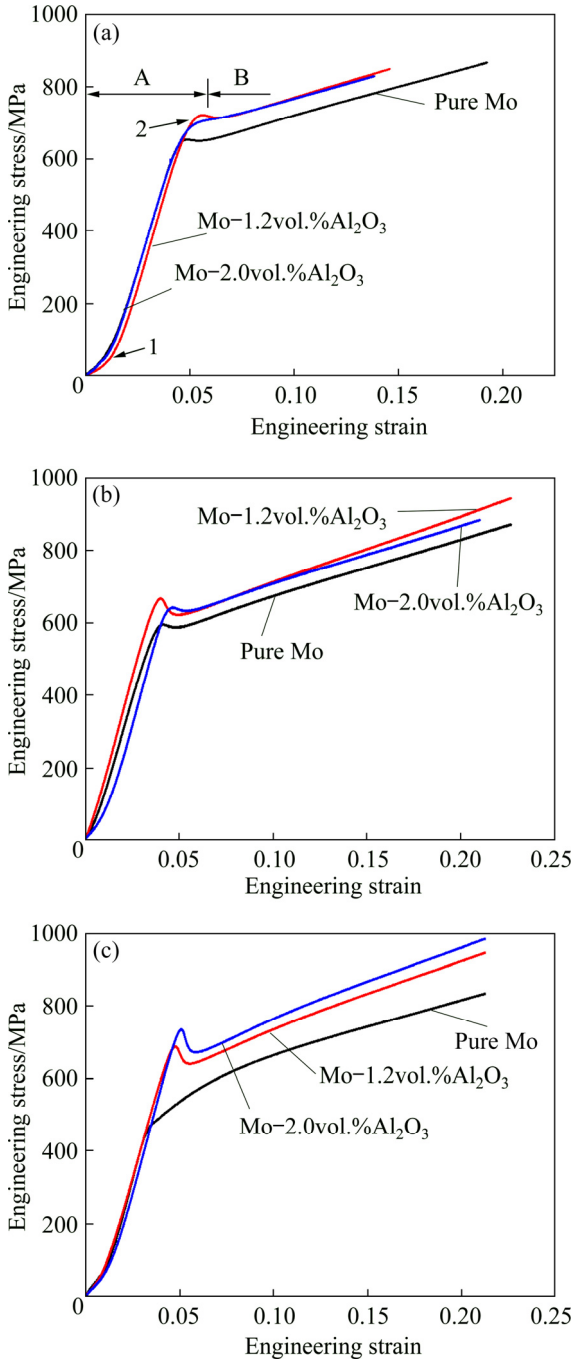

Fig. 12 Compression engineering stress−strain curves of Mo−Al_2O_3 alloys: (a) As-swaged; (b) Annealed at 850 °C; (c) Annealed at 1200 °C

increases and then decreases, whereas that of samples annealed at 1200 °C increases only. As shown in Fig. 13, the Mo−1.2vol.%Al_2O_3 alloys obtained after swaging and 850 °C annealing possess high compression yield strengths of (718±17) MPa and (660±18) MPa, respectively, whereas the compression yield strength of the Mo−2.0vol.% Al_2O_3 alloy annealed at 1200 °C is (710±15) MPa. The yield strengths of these samples

increase by 11.5%, 12.1% and 56.0%, respectively, compared with the yield strength of pure Mo under the same conditions, indicating that the mechanical properties of Mo alloys are remarkably improved by Al_2O_3 doping.

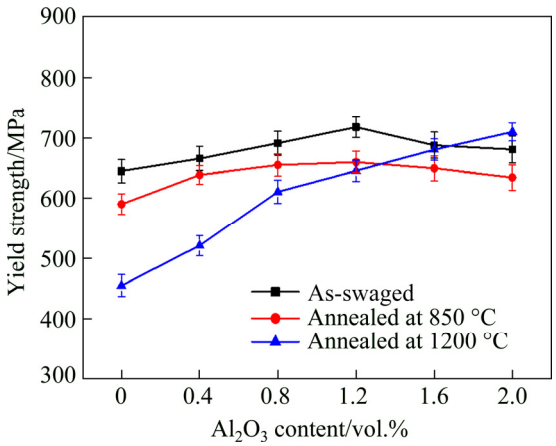

Fig. 13 Compression yielding strength of Mo−Al_2O_3 alloys

The Mo alloy specimens show a drum shape after compression due to their excellent ductility. Figure 14 shows TEM images taken from different deformation zones of Mo−2.0vol%Al_2O_3 specimen after compression test. The images reveal that the microstructural evolution of the alloy may be related to the formation of sub-grains in the severe deformation zone during compression. In the partial deformation zone (Fig. 14(a)), the fracture of individual Mo grains, which may be due to stress concentration during compression, can easily be observed by using TEM. As the strain continues to increase, the dislocation pattern changes remarkably compared with that in the partial deformation zone. During compression deformation, dislocation lines (Fig. 8(c)) tend to coalesce, intersecting dense dislocation walls (DDWs). The dislocation cell network in Fig. 14(b) reflects the regular alignment of intersecting DDWs along the shear plane. As plastic strain accumulates, these DDWs multiply and form an evident intersecting structure through self-organized dislocation activities, resulting in a balanced low-energy dislocation structure that is frequently found in steel materials [34,35]. A fully-developed intersecting structure is shown in Fig. 14(c). Ultrafine regular-shaped (parallelogram) DDWs with sizes of 50−100 nm are visible. DDWs in the original coarse grains are cut into nanoscale blocks due to shear stress and form sub-grains in the severe deformation zone. This finding provides a reference for further research on grain refinement caused by the deformation.

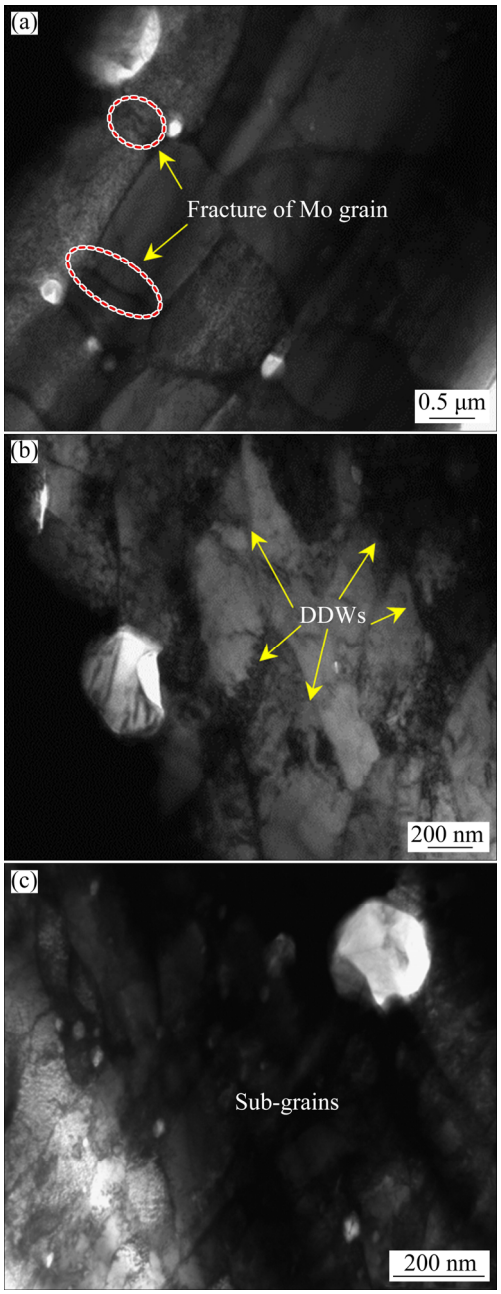

Fig. 14 Microstructures of Mo−2.0vol.%Al_2O_3 alloy after compression testing: (a) Partial deformation; (b) Deformation; (c) Severe deformation

4 Discussion

4.1 Degradation of mechanical properties of Mo alloys doped with high content Al_2O_3

According to the size of Mo grains doped with different Al_2O_3 contents, variations in the yield strength of the samples as-swaged and after 850 °C annealing deviate from a commonly assumed

regularity (Hall–Petch relationship: $\sigma_y=\sigma_0+k_y d^{-1/2}$) (Fig. 7). A few microcracks can be observed on the surface of Mo−2.0vol.%Al_2O_3 alloy (Fig. 15(a)). The width of these microcracks is approximately 0−1.5 μm (Fig. 15(b)). Initiation or termination of microcracks along Al_2O_3 particles can be seen in Fig. 15(c). However, microcracks are not found in the Mo−Al_2O_3 alloys annealed at 1200 °C. Mo grain growth results in the disappearance of microcracks during annealing at 1200 °C, which could be explained in term of the mean size of Mo particles (Fig. 7). The formation of microcracks may be attributed to the precipitation of coarse Al_2O_3 particles at Mo grain boundaries during sample preparation. During the swaging process, several dislocations are accumulated and tangle around Al_2O_3 particles due to the large deformation provided by the sintering billet (d20 mm) to the final sample (d8 mm). Hence, coarse particles at Mo grain boundaries induce severe micro-stress/strain concentration, which results in a mechanical mismatch between the matrix and particles, and microcracks are initiated around coarser particles. This finding has also been observed in the MZ-17 alloy reported by SILVA et al [36]. Small microcracks join to form large microcracks along Mo grain boundaries with increasing the deformation of Mo alloy. The process of microcrack formation is illustrated in Fig. 16. During compression, microcracks existing in the Mo−Al_2O_3 alloys act as a crack source and cause the alloy to fail rapidly.

4.2 Effects of Al_2O_3 particles on Mo alloy properties

The Al_2O_3 particles are formed at different scales during sample preparation. Small secondary-phase particles distribute in the Mo grains, whereas coarse-phase particles appear on Mo grain boundaries. The Al_2O_3 particles distributing in Mo intracrystalline and intercrystalline can effectively pin and prevent the movement of Mo grains to achieve grain refinement. The grains of pure Mo samples quickly grow at high temperature, but the growth of Mo−Al_2O_3 grains is slow, thus indicating that the recrystallization temperature of Mo alloys can be improved by doping with Al_2O_3 particles. The grain size of the matrix decreases with increasing volume fraction of the doping phase, but the mechanical properties of Mo alloys are not as expected due to the presence of microcracks.

The strength and plasticity of materials are important mechanical property indices related to dislocations in the matrix. During compression of

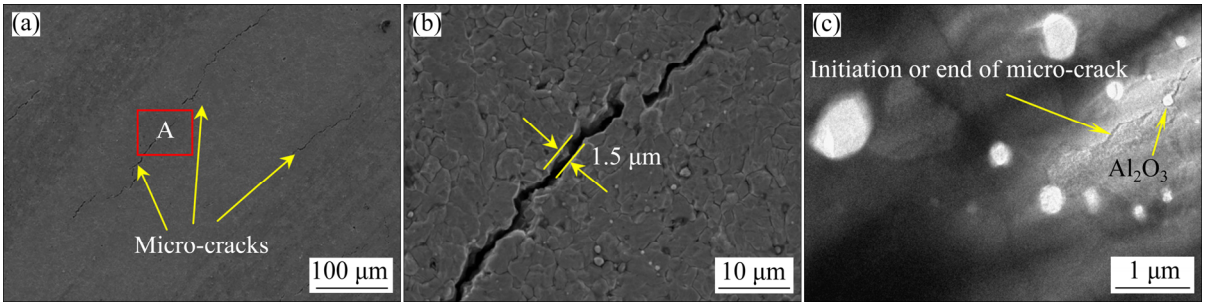

Fig. 15 Micrographs of swaged Mo−2.0vol.%Al_2O_3 alloy: (a) SEM image; (b) Area A; (c) TEM image

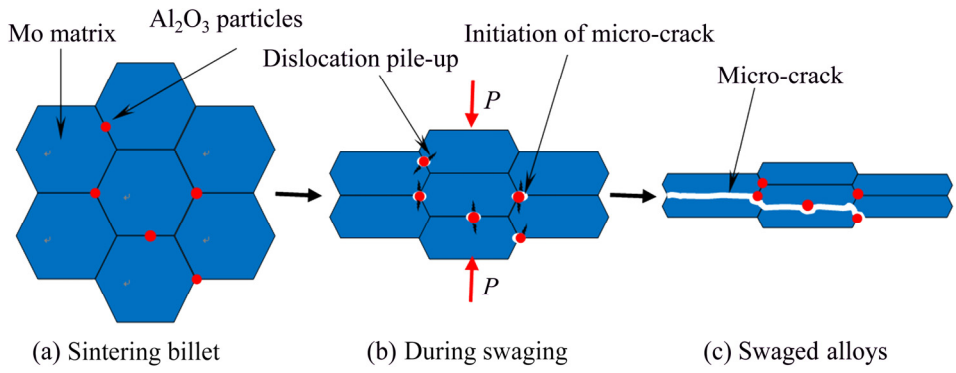

Fig. 16 Schematic diagram of micro-cracks produced in Mo−2.0vol.%Al_2O_3 alloy during swaging process

polycrystalline materials, various dislocation activities in the matrix, including sliding, accumulation, interaction, tangling and spatial rearrangement, normally occur to accommodate plastic strain. The Al_2O_3 particles can effectively prevent dislocation motion as strain accumulates. In addition, dislocation annihilation and rearrangement occur around secondary-phase particles to minimize the total system energy, resulting in the production of more DDWs. These DDWs gradually transform into sub-boundaries separating individual cells (Fig. 14), which are finally transformed into sub-grains that could further enhance/improve the strength and plasticity of the Mo alloys. The crystallographic relationship between Al_2O_3 and the Mo matrix (Fig. 10(c)) can also improve the strength and plasticity of the resultant alloys, as confirmed in previous work [27].

5 Conclusions

(1) After sintering, the Al_2O_3 particles are stabilized in the Mo matrix in the form of α crystals. As the Al_2O_3 content increases from 0 to 2.0 vol.%, the grain size of the Mo alloys remarkably decreases. Among the samples synthesized, the swaged Mo−2.0vol.%Al_2O_3 alloy shows the finest microstructure with an average grain size of 2.5 μm.

(2) The Al_2O_3 particles show a typical hexagonal close-packed (hcp) atomic stacking mode, which is characteristic of α-Al_2O_3. An amorphous transition layer with dimensions of 3−8 nm exists between α-Al_2O_3 and the Mo matrix. The crystallographic orientations at the interface are $[\bar{1}11]_{\alpha\text{-}Al_2O_3} // [\bar{1}11]_{Mo}$ and $(1\bar{1}2)_{\alpha\text{-}Al_2O_3} // (0\bar{1}1)_{Mo}$.

(3) Microcracks appear in the Mo−Al_2O_3 alloys with increasing Al_2O_3 content. Existing microcracks in the Mo−Al_2O_3 alloys act as a crack source and cause the alloy to fail rapidly during compression.

(4) The elastic modulus, nano-hardness and compression yield strength of the Mo alloys are improved by addition of Al_2O_3. The compression yield strength of the swaged Mo−1.2vol.%Al_2O_3 alloys, Mo−1.2vol.%Al_2O_3 alloys annealed at 850 °C and Mo−2.0vol.%Al_2O_3 annealed at 1200 °C is approximately 11.5%, 12.1% and 56.0% higher than that of pure Mo alloys. Improvements in the mechanical properties of the Mo alloys could be attributed to secondary-phase and dislocation strengthening.

References

[1] KOK Y, TAN X P, WANG P, NAI M L S, LOH N H, LIU E, TOR S B. Anisotropy and heterogeneity of microstructure and mechanical properties in metal additive manufacturing: A critical review [J]. Materials & Design, 2017, 139: 565−586.

[2] XU Liu-jie, WEI Shi-zhong, LIU Qiang, ZHANG Guo-shang, LI Ji-wen. Microstructure and high-temperature frictional wear property of Mo-based composites reinforced by aluminum and lanthanum oxides [J]. Tribology Transactions, 2013, 56: 833−840.

[3] CAO Hua-zhen, TONG Cheng-jian, ZHANG Hui-bin, ZHENG Guo-qu. Mechanism of MoO_2 electrodeposition from ammonium molybdate solution [J]. Transactions of Nonferrous Metals Society of China, 2019, 29: 1744−1752.

[4] MAKUCH N, DZIARSKI P, KULKA M, PIASECKI A, TULIŃSKI M, MAJCHROWSKI R. Influence of niobium and molybdenum addition on microstructure and wear behavior of laser-borided layers produced on Nimonic 80A-alloy [J]. Transactions of Nonferrous Metals Society of China, 2019, 29: 322−337.

[5] LIU Gang, ZHANG Guo-jun, JIANG Feng, DING Xiang-dong, SUN Yun-jin, SUN Jun, MA E. Nanostructured high-strength molybdenum alloys with unprecedented tensile ductility [J]. Nature Materials, 2013, 12: 344−350.

[6] CAO Yuan-kui, LIU Yong, LIU Bin, ZHANG Wei-dong, WANG Jia-wen, DU Meng. Effects of Al and Mo on high temperature oxidation behavior of refractory high entropy alloys [J]. Transactions of Nonferrous Metals Society of China, 2019, 29: 1476−1483.

[7] HU Jian, SHI Yi-ning, SAUVAGE X, SHA Gang, LU Ke. Grain boundary stability governs hardening and softening in extremely fine nanograined metals [J]. Science, 2017, 355: 1292−1296.

[8] DUAN Bo-hua, ZHANG Zhao, WANG De-zhi, ZHOU Tao. Microwave sintering of Mo nanopowder and its densification behavior [J]. Transactions of Nonferrous Metals Society of China, 2019, 29: 1705−1713.

[9] YAO Li-ying, WEI Shi-zhong, ZHOU Yu-cheng, XU Liu-jie, CHEN Chong, SUN Tie-long, SHI Peng-peng. Preparation and characterization of Mo/ZrO_2−Y_2O_3 composites [J]. International Journal of Refractory Metal and Hard Materials, 2018, 75: 202−210.

[10] WANG Jin-shu, LIU Wei, LI Hong-yi, GAO Fei, REN Zhi-yuan, ZHOU Mei-ling. Emission property of Y_2O_3-doped Mo secondary emitter [J]. Transactions of Nonferrous Metals Society of China, 2010, 20: 233−237.

[11] EL M S, TOURNIER J M. A review of refractory metal alloys and mechanically alloyed-oxide dispersion strengthened steels for space nuclear power systems [J].

Journal of Nuclear Materials, 2005, 340: 93−112.

[12] WADSWORTH J, NIEH T G, STEPHENS J J. Recent advances in aerospace refractory metal alloys [J]. International Materials Reviews, 1988, 33: 131−150.

[13] ZHANG Jiu-xing, LIU Lu, ZHOU Mei-ling, HU Yan-chao, ZUO Tie-yong. Fracture toughness of sintered Mo−La_2O_3 alloy and the toughening mechanism [J]. International Journal of Refractory Metals and Hard Materials, 1999, 17: 405−409.

[14] LORIA E A. Methods for improving the ductility of molybdenum [J]. Journal of the Less Common Metals, 1967, 12: 425−428.

[15] CHENG Pi-ming, ZHANG Guo-jun, ZHANG Jiu-xing, LIU Gang, SUN Jun. Coupling effect of intergranular and intragranular particles on ductile fracture of Mo−La_2O_3 alloys [J]. Materials Science and Engineering A, 2015, 640: 320−329.

[16] ZHANG Guo-jun, SUN Yuan-jun, ZUO Chao, WEI Jian-feng, SUN Jun. Microstructure and mechanical properties of multi-components rare earth oxide-doped molybdenum alloys [J]. Materials Science and Engineering A, 2008, 483: 350−352.

[17] YANG Xiao-qing, TAN Hua, LIN Nan, LI Zhi-xiang, HE Yue-hui. Effects of the lanthanum content on the microstructure and properties of the molybdenum alloy [J]. International Journal of Refractory Metals and Hard Materials, 2016, 61: 179−184.

[18] CUI Chao-peng, GAO Yi-ming, WEI Shi-zhong, ZHOU Yu-cheng, ZHU Xiang-wei. Microstructure and high temperature deformation behavior of the Mo−ZrO_2 alloys [J]. Journal of Alloys and Compounds, 2017, 716: 321−329.

[19] CUI Chao-peng, ZHU Xiang-wei, LIU Shu-long, LI Qiang, ZHANG Min, ZHU Guang-ping, WEI Shi-zhong. Effect of nano-sized ZrO_2 on high temperature performance of Mo−ZrO_2 alloy [J]. Journal of Alloys and Compounds, 2018, 768: 81−87.

[20] RAHAMAN M N, YAO A, BAL B S, GARINO J P, RIES M D. Ceramics for prosthetic hip and knee joint replacement [J]. Journal of the American Ceramic Society, 2007, 90: 1965−1988.

[21] SHON I J. Rapid consolidation of nanostructured Mo−Al_2O_3 composite from mechanically synthesized powders [J]. Ceramics International, 2018, 44: 2587−2592.

[22] ZHOU Yu-cheng, WEI Shi-zhong, XU Liu-jie, LI Xiu-qing. Research on high-temperature properties of the molybdenum sheet doped with 1.0 wt% Al_2O_3 particles [J]. Journal of Alloys and Compounds, 2018, 769: 340−346.

[23] CHEN Chang, TAN Wang, WANG Ming-pu, LI Zhou, LEI Qian, XIA Fu-zhong. The transverse elongation and fracture mechanism of the upset Mo and Mo−La_2O_3 bars [J]. Materials Science and Engineering A, 2010, 527: 600−605.

[24] WADSWORTH J, MORSE G R, CHEWEY P M. The microstructure and mechanical properties of a welded molybdenum alloy [J]. Materials Science and Engineering A, 1983, 59: 257−273.

[25] WANG Chang-ji, ZHANG Lai-qi, WEI Shi-zhong, PAN Kun-ming, WU Xiao-chao, LI Qing-kui. Preparation, microstructure, and constitutive equation of W−0.25wt.%Al_2O_3 alloy [J]. Materials Science and Engineering A, 2019, 744: 79−85.

[26] SCATTERGOOD R O, BACON D J. The Orowan mechanism in anisotropic crystals [J]. Philosophical Magazine, 1957, 31: 179−198.

[27] XU Liu-jie, WEI Shi-zhong, ZHANG Dan-dan, LI Yan, ZHANG Guo-shang, LI Ji-wen. Fine structure and interface characteristic of α-Al_2O_3 in molybdenum alloy [J]. International Journal of Refractory Metals and Hard Materials, 2013, 41: 483−488.

[28] TURNBULL D, VONNEGUT B. Nucleation Catalysis [J]. Industrial & Engineering Chemistry Research, 1952, 44: 1292−1298.

[29] DINI G, R. UEJI R, NAJAFIZADEH A, MONIR S M. Flow stress analysis of TWIP steel via the XRD measurement of dislocation density [J]. Materials Science and Engineering A, 2010, 527: 2759−2763.

[30] SMALLMAN R E, WESTMACOTT K H. Stacking faults in face-centred cubic metals and alloys [J]. Philosophical Magazine, 1957, 2: 669−683.

[31] LIU Rui-ping, WANG Shao-feng, WANG Rui, JIAO Jian. The theoretical investigations of the core structure and the Peierls stress of the 1/2⟨111⟩{110} edge dislocation in Mo [J]. Materials Science and Engineering A, 2010, 527: 4887−4890.

[32] LUTTEROTTI L, GIALANELLA S. X-ray diffraction characterization of heavily deformed metallic specimens [J]. Acta Materialia, 1998, 46: 101−110.

[33] OLIVER W C, PHARR G M. Measurement of the hardness and elastic modulus by instrumented indentation: Advances in understanding and refinements to methodology [J]. Journal of Materials Research, 2004, 19: 3−20.

[34] ZHANG Lai-chang, CALIN M, PATURAUD F, ECKERT J. Deformation-induced grain refinement in body-centered cubic Co−Fe alloys upon room temperature compression [J]. Materials Science and Engineering A, 2010, 52: 5796−5800.

[35] TAO Nai-rong, WANG Zhen-bo, TONG W P, SUI Man-ling, LU J, LU Ke. An investigation of surface nanocrystallization mechanism in Fe induced by surface mechanical attrition treatment [J]. Acta Materials, 2002, 50: 4603−4616.

[36] SILVA E Z, KESTLER H, SANDIM H R Z. Particle-stimulated nucleation of recrystallization in the hot-deformed molybdenum alloy MZ-17 [J]. International Journal of Refractory Metals and Hard Materials, 2018, 73: 74−78.

Al_2O_3 颗粒弥散强化钼合金的显微组织与压缩性能

孙铁龙[1]，徐流杰[1]，魏世忠[2]，潘昆明[1]，李武会[1]，周玉成[2]，黄志民[3]

1. 河南科技大学 河南省高温结构与功能材料重点实验室，洛阳 471003；
2. 河南科技大学 国家金属材料磨损控制与成型联合工程研究中心，洛阳 471003；
3. 厦门钨业股份有限公司 中国钨科技研发中心，厦门 361000

摘 要：采用水热合成法和粉末冶金方法制备 Al_2O_3 颗粒增强 Mo 合金，并利用 XRD、SEM 和 TEM 对所制备的 Mo−Al_2O_3 合金的显微组织进行研究。结果表明，Al_2O_3 颗粒以稳定的六方相(α-Al_2O_3)形式均匀地分布在 Mo 基体中，超细 α-Al_2O_3 颗粒显著细化 Mo 合金的晶粒尺寸，增加 Mo 合金位错密度。此外，α-Al_2O_3 与 Mo 晶粒间存在良好的界面结合区，且 Al_2O_3 颗粒与 Mo 基体界面存在一定的晶体学关系：$[\bar{1}11]_{\alpha\text{-}Al_2O_3}$ // $[\bar{1}11]_{Mo}$ 和 $(1\bar{1}2)_{\alpha\text{-}Al_2O_3}$ // $(0\bar{1}1)_{Mo}$。由于二次相强化效应和位错强化效应，与纯 Mo 相比，1200 °C 退火的 Mo−2.0%Al_2O_3 (体积分数)合金的屈服强度提高约 56.0%。结果表明，添加 Al_2O_3 颗粒是改善 Mo 合金力学性能的一种有效方法。

关键词：Mo−Al_2O_3 合金；水热合成；界面；压缩实验；弥散强化

(Edited by Bing YANG)